

Numerical simulation of the water desalination process based on a modified Gouy-Chapman-Stern (GCS) model for a membrane capacitive deionization (MCDI) unit

Rui Liu, Shouguang Yao*, Yan Shen, Qiqi Zhang, Zhenyu Jiang

School of Energy and Power Engineering, Jiangsu University of Science and Technology, Zhenjiang 212003, China

*E-mail: zjyaosg@126.com

Received: 5 April 2022 / *Accepted:* 9 May 2022 / *Published:* 6 June 2022

To accurately predict the dynamical behavior of the desalination process by membrane capacitive deionization (MCDI), a modified Gouy-Chapman-Stern (GCS) model is developed by considering the finite ion size effect. Three-dimensional multiphysical simulations were performed to investigate the desalination processes of MCDI units using the classical and modified GCS models. The simulation results indicated that the modified GCS model is better than the classical model in terms of feasibility and accuracy. The modified GCS model corrects the overestimation of salt removal predicted by the classical GCS model. The modified GCS model is further adopted to investigate the effects of operation conditions (inlet velocity and cell voltage) and cell geometric characteristics (thicknesses of porous electrode, spacer and membrane) on the desalination performance. The ion adsorption ratio increases with an increase in cell voltage, and the maximum ion adsorption ratio reaches 0.28 at the highest cell voltage (1.2 V). A high inlet velocity reduces the flow residence time in the spacer and affects the ion electrosorption process. In the current work, a suitable flow velocity ranges from 0.05 to 0.10 m/s. The decrease in the space thickness reduces the resistance of ion diffusion and migration in the spacer, improving the desalination performance. The ion adsorption ratio increases to 0.6 for the narrowest spacer (0.4 mm). In addition, the ion exchange membrane has a minimal effect on the desalination performance due to its small adjustable thickness range. The change in electrode thickness mainly affects the adsorption ratio at the stage of absorption tending to saturation..

Keywords: membrane capacitive deionization; electric double layer theory; desalination; numerical simulation

1. INTRODUCTION

The growing freshwater crisis is now curbing the sustainable development of human society [1], causing more people to embark on an exploration of sustainable and energy-efficient brine purification methods. Among various desalination methods, capacitive deionization (CDI) stands out due to its high-

efficiency, energy savings, pollution-free nature and simplicity [2-3]. However, the CDI desalination performance is degraded due to certain inherent limitations of CDI, such as the coion repulsion effect during the formation of electric double layers (EDLs) and the secondary adsorption effect when the electrodes regenerate [4-6]. With the development of CDI technology, the introduction of ion exchange membranes in the CDI (referred to as MCDI) [6-8] can overcome the coion repulsion effect, thus improving the energy utilization and desalination performance.

In 2006, Lee et al. [7] discovered that the salt removal rate of MCDI was approximately 19% higher than that of CDI, and that the maximum salt removal rate was 92%. Subsequently, Omoobi et al. [9] compared the performance difference between CDI and MCDI for long-term operations by performing 50 complete desalination cycles. For the quantitative analysis of the sustainability performance of CDI and MCDI, Fritz et al. [10] adopted the exergy analysis method to evaluate the energy utilization efficiency. In addition to experimental studies, Biesheuvel et al. [8,11] established a theoretical model of the MCDI adsorption process based on the classical electric double layer model, describing the ion migration process in the diffusion layer near the ion exchange membrane, and confirming the inhibition of the coion repulsion effect of the membrane. Dlugoleckia et al. [12] investigated the ion diffusion resistance in the membrane, electric double layer and diffusion boundary layer and analyzed the ion diffusion resistance for different influent concentrations and flow velocities.

Undoubtedly, an in-depth and accurate understanding of the internal mechanism of the MCDI desalination process is important for improving and optimizing the desalination performance of MCDI. However, current CDI research focuses on experimental studies of performance comparison [13-17], material synthesis of electrodes or membranes [18-21], studies and comparisons of improved models [22, 23], and basic theoretical research [24,25]. Research on the internal mechanism of the MCDI unit by multiphysics coupled numerical simulation is still rare, and previous work [26] employed the classical GCS model for the electric double layer of the MCDI unit.

The classical GCS model can provide a good foundation model for research on the (M)CDI mechanism to some extent [27]. However, the actual desalination process is too complicated, and it is unreasonable to directly apply the classical GCS model to the (M)CDI modeling. The classical GCS model assumes that ions are treated as point charges [28]. This assumption is reasonable only in the case of weak voltage and low salt concentration. As a result, the concentration distribution within the unit predicted by the GCS model may be higher than the actual possible concentration. The hypothesis that the electrode charged surface is flat and isolated will cause the GCS model to overestimate the potential and concentration of the porous surface where the electric double layer overlaps. Hence, the calculation of the (M)CDI salt removal amount is not as accurate as expected. Therefore, the GCS model needs to be modified to account for the finite ion size [29] to reduce the error in the calculation of the internal potential and concentration distribution of the (M)CDI unit. The Carnahan-Starling equation (hereafter referred to as the CS equation) [30], developed by Norman Carnahan and Kenneth Starling in 1969, is a theoretical equation that takes the finite ion size into account. The CS equation uses a dimensionless excess electrochemical potential term to describe the finite ion size by approximating the additional electrochemical potential required to concentrate a unit volume of ions [31,32]. Once the CS equation is incorporated into the GCS model, the CS equation can provide very precise adjustments for the finite ion volume effects that occur in (M)CDI.

Based on the above considerations, this paper introduces the modified electric double layer model (GCS-CS model), which can more accurately describe the mechanism of the MCDI desalination process. After verifying its applicability and accuracy, multiphysical simulations based on the GCS-CS model are performed to investigate the effects of operation conditions and cell geometric characteristics on the desalination performance of MCDIs.

2. MODEL SPECIFICATION

2.1. Geometric model and hypothesis

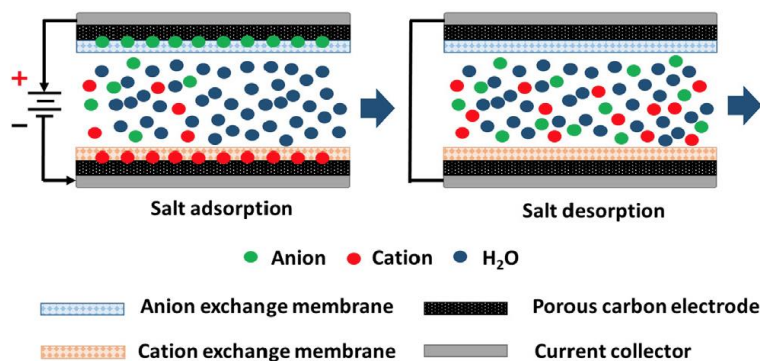


Figure 1. Schematic of MCDI

As shown in Figure 1, the current work considers the classical flow-by MCDI unit [33] as the research object. A 3D geometric model including a pair of porous carbon electrodes, anion/cation exchange membranes and the spacer channel as shown in Figure 2 is established. Figure 2(a) gives a three-dimensional view of the MCDI unit, and Figure 2(b) gives a two-dimensional view of the z-x plane. The geometric sizes of the model are shown in Table 1. The x direction is defined as the thickness direction of the MCDI unit; the y direction represents the width direction, and the main flow direction in the spacer channel is the z direction. In general, x, y, and z represent Cartesian coordinate components.

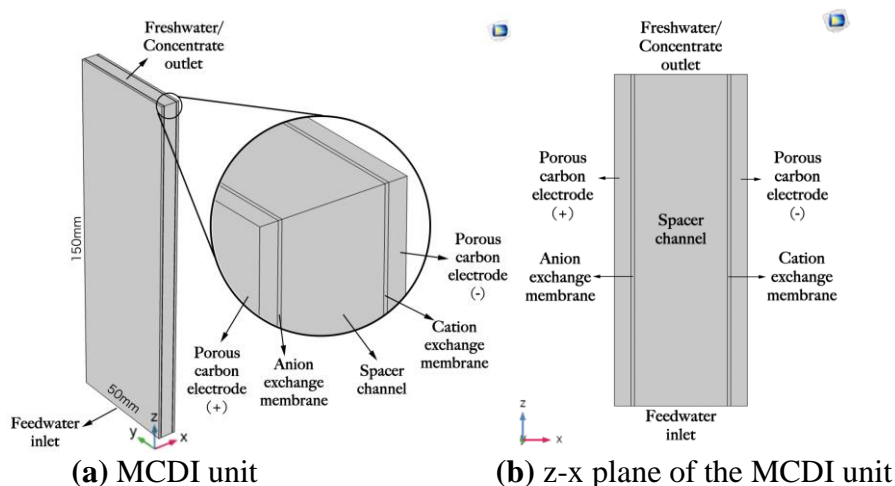


Figure 2. Geometric structure of the MCDI unit.

The following assumptions are made to simulate the salt ion adsorption and desorption process in the MCDI unit [26]:

- (1) The solution is a dilute NaCl solution, and the solute exists in a free form of monovalent anions and cations.
- (2) The flow is considered a single-phase, incompressible, low-velocity, laminar flow, and the influences of the entrance are disregarded.
- (3) The electrodes, ion exchange membranes and solutions in the unit are isotropic, and the material property parameters are constant values.
- (4) The active groups in the ion exchange membrane are evenly distributed. The fixed charge concentration is uniform, and it is considered that only one ionic conductor exists. The water molecules cannot pass alone, and the fluid flow in the membrane is not considered.
- (5) The desalination process is carried out under the applied cell voltage ($\leq 1.2V$). Only the physical process is considered, and the chemical reactions (electrolysis of water or hydrogen evolution and oxygen evolution of the electrode) are disregarded.
- (6) The target unit has no heat exchange with the outside environment, and the influence of gravity is disregarded.
- (7) The ion was deemed a sphere.

2.2. Parameter setting

The modeling parameters of the MCDI unit are set as shown in Table 1.

Table 1. Parameter settings of the MCDI unit

	Nomenclature	Unit	Value	Others
Geometric parameter	Electrode plate length L_e (in the z -axis)	mm	150	
	Electrode plate width W_e (in the y -axis)	mm	50	
	Electrode plate thickness D_e (in the x -axis)	mm	0.08	original
	Ion exchange membrane thickness D_m	mm	0.02	original
	Channel spacing D_s	mm	0.8	original
	Electrode plate porous carbon density (ρ_e)	kg/m ³	2260	
	Electrode plate conductivity (σ_e)	S/m	5000	
	Electrode plate porosity (ε_e)	-	0.4	
	Electrode plate permeability (κ_e)	-	1.0×10^{-10}	
	NaCl solution dynamic viscosity (μ_s)	Pa·s	0.003139	
Physical parameter	NaCl solution conductivity (σ_s)	S/m	1	
	NaCl solution relative dielectric constant	-	80	
	Na ⁺ diffusion coefficient (D_{Na})	m ² /s	2.5×10^{-9}	
	Cl ⁻ diffusion coefficient (D_{Cl})	m ² /s	2.0×10^{-9}	
	NaCl solution inlet concentration in (c_{in})	mol/m ³	500	
	Na ⁺ diffusion coefficient ($D_{Na,m}$) in cation exchange membrane	m ² /s	3.52×10^{-11}	
	Cl ⁻ diffusion coefficient ($D_{Cl,m}$) in anion exchange membrane	m ² /s	3.91×10^{-11}	

Operating parameter	Unit voltage (V_{unit})	V	1.2	original
	Ambient temperature (T)	K	293.15	
	NaCl solution inlet velocity (u_{in})	m/s	0.1	original
	Desorption phase start time node	s	120	

2.3. Mathematical model

The porous media flow is utilized to solve the velocity field distribution and pressure distribution of the main channel and porous electrode region. The fluid flow in the main flow channel satisfies the continuous Navier-Stokes momentum conservation equation [34] as follows

$$\nabla \cdot (\rho \mathbf{u}) = 0 \quad (1)$$

$$\rho \frac{\partial \mathbf{u}}{\partial t} + \rho (\mathbf{u} \cdot \nabla) \mathbf{u} = \mu \nabla \cdot \left[\left(\nabla \mathbf{u} + (\nabla \mathbf{u})^T \right) \right] - \nabla p \quad (2)$$

where ρ is the fluid density ($\text{kg} \cdot \text{m}^{-3}$), \mathbf{u} is the fluid velocity field vector ($\text{m} \cdot \text{s}^{-1}$), p is the internal pressure of the unit (Pa), and μ is the hydrodynamic viscosity ($\text{Pa} \cdot \text{s}$).

The fluid flow in the porous electrode region satisfies the continuous Navier-Stokes momentum conservation equation and conforms to Darcy's law.

$$\nabla \cdot (\rho \mathbf{u}) = S_i \quad (3)$$

$$\rho \frac{\partial \mathbf{u}}{\partial t} + \left(\frac{\mu}{k} + S_i \right) \mathbf{u} = \frac{\mu}{\varepsilon_p} \nabla \cdot \left[\left(\nabla \mathbf{u} + (\nabla \mathbf{u})^T \right) \right] - \nabla p \quad (4)$$

$$\mathbf{u} = -\frac{k}{\mu} \nabla p \quad (5)$$

$$k = \varepsilon_p^3 / \left[\kappa A_s^2 (1 - \varepsilon_p)^2 \right] \quad (6)$$

where S_i is the source item ($\text{kg} \cdot \text{m}^{-3} \cdot \text{s}^{-1}$) that is usually set to zero, ε_p is the porosity of the porous electrode, k is the permeability of the porous electrode, κ is the Kozeny-Carman constant, and A_s is the specific surface area (m^{-1}) of the porous electrode.

The ion transport processes in the MCDI are driven by flow convection, diffusion and electromigration. Dilute solution transport theory is applied to describe the ion mass transfer and concentration distribution of each ion. Poisson's equation is selected to solve the electrostatic field and the Nernst Planck equation is adopted to describe the ion mass transfer. The above set of equations is also known as the Nernst-Planck-Poisson (NPP) equation [35].

The relationship between the potential change and the electrode surface charge density in the unit is solved using the Poisson equation:

$$\nabla \cdot (-\varepsilon_0 \varepsilon_r \nabla \phi) = \rho_c = F(c_+ - c_-) \quad (7)$$

where $\varepsilon_0 \varepsilon_r$ is a dielectric constant, ϕ is a local potential (V), ρ_c is an electrode surface charge density ($\text{C} \cdot \text{m}^{-2}$), and c_+ and c_- represent the cation concentration and anion concentration ($\text{mol} \cdot \text{m}^{-3}$) respectively.

The ion transport in the solution is described by the NPP equation, and the ion flux J_i is described as:

$$J_i = -D_i \left(\nabla c_i + \frac{z_i F}{RT} c_i \nabla \phi \right) + \mathbf{u} c_i \quad (8)$$

where D_i is the ion diffusion coefficient ($\text{m}^2 \cdot \text{s}^{-1}$), c_i is the ion concentration ($\text{mol} \cdot \text{m}^{-3}$), z_i is the ion valence, F is the Faraday constant ($96485 \text{ C} \cdot \text{mol}^{-1}$), R is the ideal gas constant ($8.314 \text{ J} \cdot \text{mol}^{-1} \cdot \text{K}^{-1}$) and T is the temperature (K).

In the ion exchange membranes, Eq. 8 is also used to calculate the ion flux by setting the velocity to zero, as given in Eq. 9, since the flow is disregarded in the ion exchange membrane.

$$u c_i = 0 \quad (9)$$

The ion diffusion coefficient in the porous electrode region is related to the porous structure. The coefficient is corrected to the effective diffusion coefficient D_i^{eff} according to the Bruggemann modified equation as follows:

$$D_i^{\text{eff}} = \varepsilon_p^{3/2} D_i \quad (10)$$

Based on mass conservation, the ion concentration needs to satisfy:

$$\frac{\partial c_i}{\partial t} + \nabla \cdot \mathbf{J}_i = R_i \quad (11)$$

$$\nabla \cdot \mathbf{J}_i = 0 \quad (12)$$

where R_i is the reaction source term for ion adsorption or desorption. In the porous electrode and ion exchange membrane region, ion conservation needs to meet the following requirement due to the influence of porosity.

$$\frac{\partial}{\partial t} (\varepsilon_p^{\text{eff}} c_i) + \nabla \cdot \mathbf{J}_i = R_i \quad (13)$$

where $\varepsilon_p^{\text{eff}}$ is the correction factor. In addition, the fixed charge and counterion in the ion exchange membrane need to meet the condition of electroneutrality

$$\sigma_C^{\text{mem}} + \sum_i z_i c_i = 0 \quad (14)$$

$$\mathbf{j} = F \sum \mathbf{J}_i \quad (15)$$

$$\nabla \cdot \mathbf{j} = 0 \quad (16)$$

where σ_C^{mem} is the surface fixed charge density (mol/m^2) and \mathbf{j} is the current density (A/m^2) of the ion exchange membrane.

When the dilute mass transfer and electrostatic physics field are solved in the coupling manner, the electric double layer model is defined because the electric double layer is considered coupling of the Nernst-Planck equation and Poisson's equation. One of the simplest and most classic electric double layer models is the Gouy-Chapman-Stern (GCS) model, which starts with Poisson's equation of the Cartesian coordinate system. It is assumed that the electrode plates are infinite in the y and z directions, and that x starts from the surface of the electrode plates. The coupling between Poisson's equation, which describes the potential distribution, and the Boltzmann equation, which describes the concentration distribution, can obtain the following relation [34]:

$$\frac{d^2 \psi(x)}{dx^2} = 2z c_b \sinh[z(\psi(x) - \psi_b)] \frac{F}{\varepsilon_r \varepsilon_0 V_T} \quad (17)$$

where c_b is the ion concentration ($\text{mol} \cdot \text{m}^{-3}$) in the solution, $V_T = k_B T / e$ is the thermal voltage (V), z is the ionic valence charge, and $\psi(x)$ and ψ_b are the local potential and solution potential, respectively.

The relationship among the electrode applied voltage V_{cell} , potential of the electrode surface ψ_0 , Stern layer potential ψ_{St} and solution potential ψ_b is given as follows [11]:

$$\frac{V_{cell}}{2V_T} = (\psi_{St} - \psi_b) + (\psi_0 - \psi_{St}) \quad (18)$$

The voltage distribution of the Stern layer in the electric double layer is expressed as follows:

$$\left(\frac{dV}{dx}\right)_{St} = -\frac{V_{St}}{\delta} \quad (19)$$

where V_{St} is the voltage (V) on the Stern layer and δ is the thickness of the Stern layer, which is also known as the hydrated ionic radius (m).

For the classic GCS model, the capacitance of the Stern layer C_{St} can be determined as

$$C_{St} = \frac{\epsilon_r \epsilon_0 A_s}{\delta} \quad (20)$$

To determine the charge on the electrode surface, it is assumed that the charge is equal to the sum of the charge on the surface of the Stern layer and that on the diffusion layer according to the principle of electric neutrality

$$4z\lambda_d c_{ex,b} \sinh\left(\frac{1}{2}z(\psi_{St} - \psi_b)\right)F = C_{St}V_T(\psi_0 - \psi_{St}) \quad (21)$$

where λ_d is the Debye length (m) and $c_{ex,b}$ is the surface excess salt concentration (mol/m²). To apply the correction of the finite ion size effect based on the Carnahan-Starling equation of state, the basic framework needs to be established. According to the GCS model, the local charge in the Stern layer can be expressed as

$$\sigma_C = 4c_b \lambda_d \sinh\left(\frac{\psi_{St} - \psi_b}{2}\right) \quad (22)$$

The charge in the Stern layer and diffusion layer are equal to the charge on the electrode surface, which satisfies the electric neutral condition. The capacitance of the Stern layer is expressed as follows:

$$C_{St}V_T(\psi_0 - \psi_{St}) = \sigma_C F \quad (23)$$

Poisson's equation and the electrochemical equilibrium equation of ions are expressed as follows:

$$\frac{d^2\psi(x)}{dx^2} = -\frac{F}{\epsilon_r \epsilon_0 V_T}(c_+ - c_-) \quad (24)$$

$$\ln c_i(x) + z_i \psi(x) + \xi_{ex,x} = \ln c_b + \xi_{ex,b} + \psi_b \quad (25)$$

The electrochemical equilibrium equation correlates the local ion concentration $c_i(x)$ to the solution ion concentration c_b by the balance among the supplied voltage, local excess electrochemical potential $\xi_{ex,x}$ and excess electrochemical potential $\xi_{ex,b}$ of the solution. The excess electrochemical potential term is determined by the volume fraction of ions. When the volume fraction of ions is large, the excess electrochemical potential is large. This item explains the difficulty of filling ions, which consumes a portion of the applied potential. This excess electrochemical potential term determined by the CS equation of state is described here. The excess electrochemical potential at a given location is given as

$$\xi_{ex} = \eta \frac{8 - 9\eta + 3\eta^2}{(1 - \eta)^3} \quad (26)$$

$$\eta = v(n_+ + n_-) = \frac{\pi d_{ion}^3}{6}(n_+ + n_-) \quad (27)$$

$$v = \frac{\pi d_{ion}^3}{6} \quad (28)$$

In the above formulas, η is a partial ion fraction. v represents the volume of one ion, and d_{ion} refers to the ion diameter. n_+ and n_- are the quantitative concentrations of cations and anions, respectively.

According to the ion distribution in the GCS-CS model corrected by the Carnahan-Starling equation of state, the ion concentration $c_i(x)$ from the electrode charging surface to any given distance x is given by the previously described ion chemical equilibrium (Eq. 25).

Next, the total ion concentration c_i ($\text{mol}\cdot\text{m}^{-3}$) from the surface to x is expressed as follows:

$$c_i = 2c_b e^{(\xi_{ex,b} - \xi_{ex,x})} \cosh(\psi(x) - \psi_b) \quad (29)$$

The local charge concentration $\sigma_C(x)$ ($\text{mol}\cdot\text{m}^{-3}$) is

$$\sigma_C(x) = -2zc_b e^{(\xi_{ex,b} - \xi_{ex,x})} \sinh z(\psi(x) - \psi_b) \quad (30)$$

The surface distribution of the porous structure of the electrode can be determined by replacing the local charge concentration with the complete Poisson-Boltzmann equation, as follows:

$$\frac{d^2\phi}{dx^2} = \left[2zc_b e^{(\xi_{ex,b} - \xi_{ex,x})} \sinh(z\phi(x)) \right] \frac{F}{\epsilon_r \epsilon_0 V_T} \quad (31)$$

The dimensionless potential on the Stern plane is expressed as follows:

$$\psi_{St} = \psi_0 - \frac{\sigma_{St} d_{ion} FSA}{2C_{St} V_T} \quad (32)$$

This series of modeling formulas are GCS-CS models, and there is no analytical solution, so they must be numerically solved. The boundary condition is that the potential of the Stern plane is equal to the ψ_{St} calculated from the charge distribution, and the solution potential ψ_b far from the electrode plate is equal to zero.

2.4. Boundary conditions

(1) Concentration boundary conditions:

At the inlet, the concentration c_i of each component is constant, such as

$$c_{bulk}^{in} = c_+^{in} = c_-^{in} = 500 \text{ mol}/\text{m}^3 \quad (33)$$

At the outlet, the flux of each component is zero, i.e.,

$$-\mathbf{n} \cdot D_i \nabla c_i = 0 \quad (34)$$

(2) Velocity boundary conditions:

The constant velocity is set at the inlet, i.e.,

$$u = u_{in} = 0.1 \text{ m}/\text{s} \quad (35)$$

The nonslip boundary condition is applied at the fluid-solid interface, i.e., the velocity (or relative velocity) of the fluid at the wall is zero.

(3) Electric potential boundary conditions:

A constant cell voltage is applied, that is,

$$\phi_+ - \phi_- = V_{cell} = 1.2V \quad (36)$$

The potential of the Stern plane ($x=\delta$) of the electric double layer is ϕ_{St} , and the potential away from the charged surface of the electrode ϕ_b is zero, that is,

$$\begin{cases} \phi(\delta) = \phi_{St} \\ \phi(\infty) = \phi_b = 0 \end{cases} \quad (37)$$

3. VALIDATION AND ANALYSIS

3.1. Comparison of the two models

Based on the classical and modified electric double layer models, simulations of MCDI are performed under the same conditions and parameters given in Table 1. The simulation results of the effluent concentration obtained from the two electric double layer models are compared and shown in Figure 3. In addition, there is also a modified Donna model (mD) [36] for comparison. The variations in effluent concentrations with time are generally consistent between the modified model and the mD model. After charging, the effluent concentration rapidly drops to the lowest point within 5 s and gradually increases to the value of the inlet concentration at 120 s.

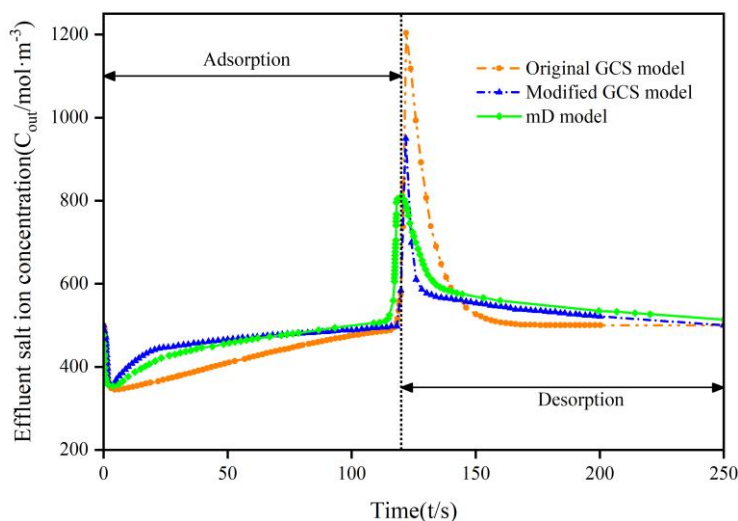


Figure 3. Curve diagram of salt ion concentration in effluent with time

After the effluent concentration reaches the lowest point, the concentration increasing rate of the original model is basically kept constant, while the concentration increasing rate of the modified GCS model and mD model gradually slows. The original GCS model assumes that ions are point charges so that the ions can continuously and infinitely move near the Stern plane. As a result, the ion adsorption rate remains constant, that is, the rate of rise of the effluent salt concentration curve is nearly constant. The applicable range of the original GCS model may exceed the limit of the thermal voltage even though

it considers the Stern layer of the electric double layer. The GCS-CS modified model considers the finite volume effect of ions. With the volumetric ions enriched in the electric double layer of the electrode surface, the absorbable volume is gradually reduced and the ion migration resistance is further increased due to the expulsion of ions with the same charge. Thus, the ion adsorption rate predicted from the modified model decreases in the late stage.

In addition, the minimum effluent concentration of the classic model can reach 343.23 mol/m^3 , while the minimum effluent concentration of the modified model is 360.67 mol/m^3 . The original model assumes that ions are point charges, which makes it suitable for applications where the voltage applied to the (M) CDI device is less than or slightly greater than the thermal voltage (applied voltage of approximately 25.7 mV). However, the voltage selected in the simulation calculation is 1.2 V for general engineering applications or experiments, which is equivalent to 0.6 V applied to the electric double layer of each electrode. This value is more than 20 times the thermal voltage. This voltage is much higher than the allowable voltage value in the classic GCS model, so the predicted concentration distribution within the unit will be higher than the actual possible concentration. The assumption of a flat and isolated electrode charged surface is effective only when a slit-like porous electrode with an infinite width and length is utilized. Notably, the carbon material used as the electrode is more complex in morphology than this porous electrode and contains a variety of geometrical pores. This porous surface morphology causes a substantial overlap of the diffusion layer. Thus, the potential and concentration at these locations as well as the salt removal of (M)CDI will be overestimated by the original GCS model.

The desorption process is achieved by removing the applied cell voltage. In the beginning of the desorption process, the effluent concentration rapidly rises to the highest point. At this time, the extremely high concentration gradient between the flow channel and the electrode is the main driving force for ion diffusion. The electric double layers formed in the electrodes disappear with the rapid desorption of ions. The effluent concentration predicted by the classical GCS model is higher than that obtained by the modified model. This is also an indirect proof that the ion adsorption is overestimated by the classical GCS model in the adsorption phase. Afterward, the effluent concentration drops rapidly, and the difference in ion concentration between the electrode region and the main channel decreases. Next, the concentration decreasing rate gradually slows, and the final concentrations of inflow and effluent water remain constant, that is, the desorption equilibrium state is reached.

3.2. Fitting tests of models

A comparison of the effluent concentration curves predicted by the two models in Figure 3, reveals that the modified model seems to be more realistic than the classical model, and more consistent with the description and prediction of the revised theory. Below, the verification is provided.

Based on previous work [8,37], the results of the MCDI experiment are fitted by a kinetic equation and an adsorption isothermal curve from the perspective of adsorption kinetics/thermodynamics, and the credibility of the modeling results is confirmed by the high correlation coefficient. Therefore, the correctness of the model is indirectly verified by testing the conformity with the adsorption kinetic/thermodynamic equation.

Table 2. Fitting results of adsorption kinetics and adsorption thermodynamic equations

Verification equation	Comparison model	Simulation parameters		Correlation coefficient
Quasi-1st-order kinetic equation $q = q_e(1 - e^{-K_1 t})$	(1)	q_e	K_1	R_1^2
	Classical model	18.4098	0.5859	0.9699
	Modified model	17.2447	0.5906	0.9864
Quasi-2nd-order kinetic equation $q = \frac{q_e^2 K_2 t}{1 + q_e K_2 t}$	(2)	q_e	K_2	R_2^2
	Classical model	19.2836	0.0056	0.9471
	Modified model	22.9938	0.0008	0.9625
Langmuir adsorption isotherm $q_e = \frac{q_{max} K_L C_e}{1 + K_L C_e}$	(3)	q_m	K_L	R_L^2
	Classical model	15.516	0.0347	0.9876
	Modified model	13.455	0.0360	0.9921
Friendlies adsorption isotherm $q_e = K_F C_e^{1/n}$	(4)	n	K_F	R_F^2
	Classical model	46.489	0.1811	0.9479
	Modified model	50.667	0.2103	0.9640

Table 2 shows the fitting results. By comparing the fitting results of the adsorption kinetic equation, the correlation coefficients of the classical and modified models satisfy $R_1^2 > R_2^2$, indicating that the fitting result of the quasi-first-order kinetic equation is better than that of the quasi-second-order kinetic equation, which corresponds to the experimental results [38]. The adsorption process of these two models is more consistent with the characteristics of the first-order reaction. However, the fitting correlation coefficient of the modified model R_2^2 is higher than that of the classical model and achieves a better fitting result, indicating that the simulated adsorption process is more accurate.

By comparing the fitting results of the adsorption thermodynamic equation $R_L^2 > R_F^2$, the modified model can better conform to the Langmuir adsorption isotherm equation. The adsorption isotherm equation seems to follow a single layer of adsorption. However, note that a single physical adsorption curve model, such as the Langmuir isotherm, is only utilized as a fitting reference. Although the data of the model simulation are very consistent with the Langmuir isotherm, the isotherm does not consider the electric double layer effect and potential driving force of ion transport [39].

In summary, it can be seen from the above correlation coefficient R^2 that the fitting result of the modified GCS-CS model is optimal. Therefore, the modified electric double layer model proposed in this work can more accurately describe the mechanism of the MCDI desalination process, and is more suitable for numerical analysis of the desalination process in MCDI unit.

4. COUPLING ANALYSIS OF THE MODIFIED MODEL

4.1. Analysis of the ion concentration field

Figure 4 shows the concentration field distributions at 0.5 s and 2.0 s in the MCDI unit during the adsorption process and the variations in concentration with time in the adsorption-desorption cycle. Figure 4(a) shows the concentration distribution at 0.5 s in the MCDI unit after the solution with a concentration of 500 mol/m³ flows into the unit. Figure 4(b) shows the concentration distribution in the MCDI at 2.0 s. It can be seen that the concentration in the space is low and that the concentration is high in the porous electrode due to ion adsorption in the electric double layers formed in porous electrodes. Figure 4(c) shows the variation in effluent concentration as a function of time, and Fig. 4(d) shows the variation in ion concentration in porous electrodes as a function of time.

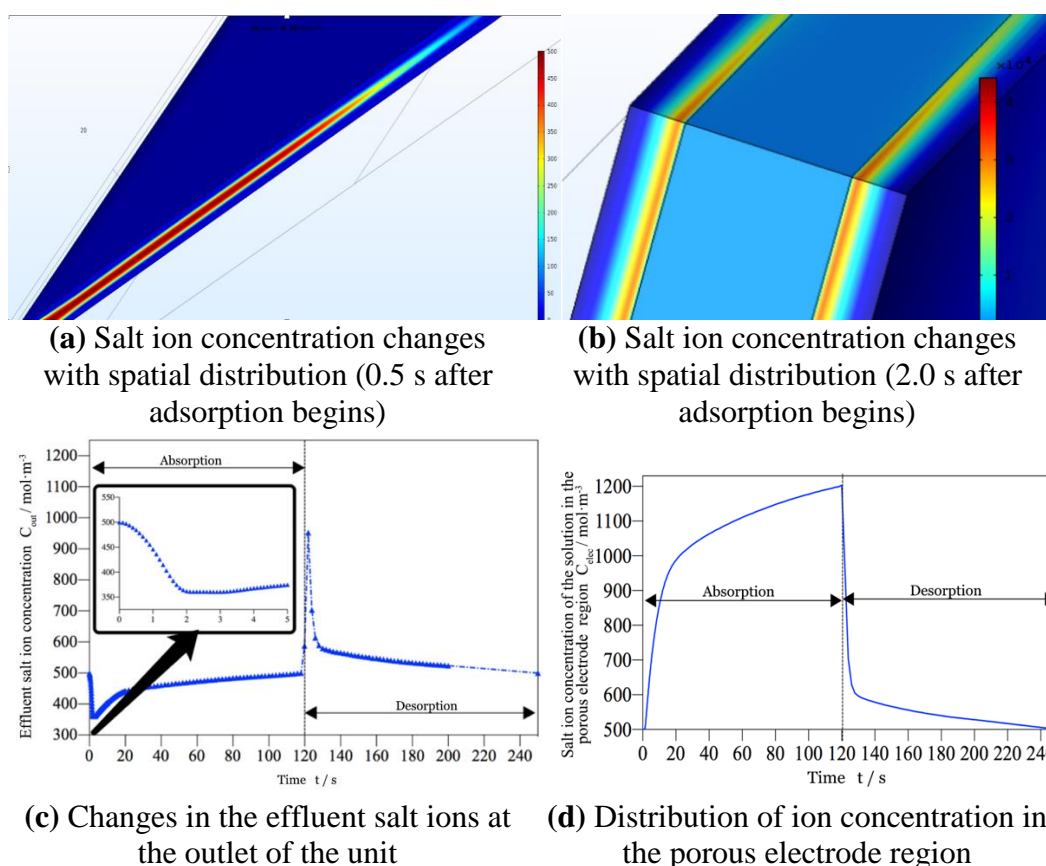


Figure 4. The concentration field distribution nephogram and concentration curve at 0.5 s and 2.0 s after adsorption begins in the MCDI unit

Figure 4(a) shows that the salt concentration in the spacer channel is much higher than that in the porous electrode and the membrane in the beginning of desorption at 0.5 s. The diffusion coefficient in the porous electrode is smaller than that in the spacer, causing an indistinct change in concentration in the porous electrode at the beginning of adsorption. The ion concentration distribution is mainly affected

by convection. Subsequently, the ions gradually diffuse into the porous electrode region and become concentrated at the electrode surface under a combination driving force of electric field and concentration gradients. At this time, the ion concentration decreases in the spacer channel and increases at the electrode surface. The concentration distribution in the MCDI shows the characteristics of low concentration in the spacer channel region and high concentration in the electrode region as shown in Figure 4(b). In addition, the seepage velocity inside the electrode is low due to the complex pore structure, small pores of the porous electrode and selective permeability of the ion exchange membrane. The ions are difficult to diffuse to the electrode plate away from the spacer channel side. Therefore, the ion concentration away from the channel side is very low.

According to the partial enlargement of the first 5 s after adsorption begins in Figure 4(c), the ions adsorbed on the surface of the electrode are not attracted to the opposite ions by the opposite polarity, because the solution in the spacer channel acts on the electric field force and the ion membrane exists, effectively preventing the coion repulsion effect. At this time, the ions in the solution start to be largely directed and steadily migrate to the electrode surface, while only a small number of ions migrate into the interior of the electrode. In the first 5 s, the selective permeability of the ion exchange membrane and the small porosity of the porous electrode generate a slow diffusion rate in the pores of the electrode. After 5 s, the large concentration gradient on the surface of the electrode and inside the electrode accelerates the ion diffusion rate in the pores of the electrode. However, at this time, the diffusion of ions from the flow channel to the electrode surface gradually slow due to a decrease in the difference in the concentration of the electrode and flow channel. Therefore, the concentration of the effluent salt in the outlet of the spacer channel rapidly decreases to approximately 350 mol/m^3 (at 2 s) and slowly rises again, as shown in Figure 4(c). Accordingly, the salt ion concentration in the porous electrode region rapidly increases, and the increasing tendency subsequently slows, as shown in Figure 4(d). The curve trends of the effluent salt concentration are correlated to the experimental results [40,41]. In addition, the time to reach saturation during the adsorption process is approximately 120 s.

Desorption is achieved by setting the applied cell voltage to zero. During the desorption process, ions on the surface of the electrode are desorbed under the concentration gradient. The high concentration difference between the electrode and the spacer accelerates the desorption of ions. As the salt concentration in the electrode region decreases, the ion concentration in the spacer channel continuously returns to the initial level, and electrode regeneration is achieved. The highest concentration in the porous electrode region is almost 1200 mol/m^3 when the ion adsorption amount is saturated. This value is higher than the highest water concentration (approximately 900 mol/m^3) in the desorption phase because the ion desorption of the porous electrode region is not instantaneously completed but is continuously performed under the concentration gradient.

4.2. Analysis of electric field potential

Figure 5(a), (b) and (c) show the distributions of electric field potential in the positive and negative electrodes and in the flow channel at 0.5 s after adsorption begins in the MCDI unit.

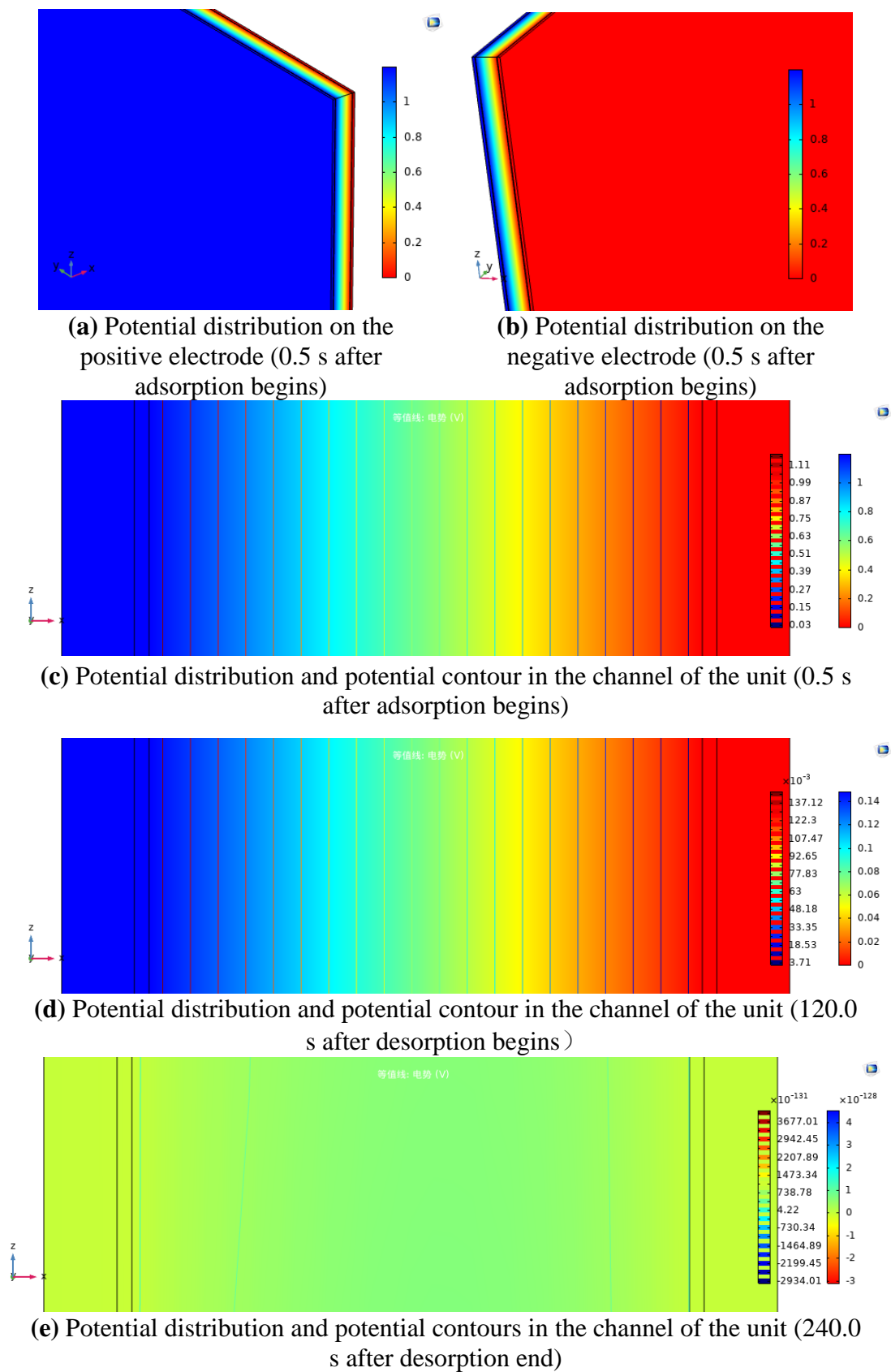


Figure 5. Electric field and potential contour distribution of the MCDI unit

Figure 5(d) and (e) show the potential distribution and potential contours in the intermediate flow channel at 120.0 s (desorption begins) and at 240.0 s (later desorption period) in the desorption process under zero voltage.

Figure 5 shows that in the MCDI adsorption stage, under an applied voltage within 0.5 s, the positive electrode potential is the largest, 1.2 V, and the negative electrode potential is the smallest, 0 V. The porous electrode material has a high electrical conductivity and a small electrical resistance, so the voltage drop is small. The potential of the spacer region gradually decreases from the positive electrode plate to the negative electrode plate. The nanoscale electric double layer effect on both sides of the flow channel is extremely weak under this macroscopic electric field. Therefore, the effect of the ion charge enriched in the electric double layer on the potential distribution is small and unsuitable for mapping. However, this effect on the diffusion and spatial distribution of the electric field is actually present. According to the modified model, we can predict that the potential of the ions in the electric double layer is exponentially decreasing along the direction away from the electrode that adsorbs it and that the near surface potential of the electrode is approximately equal to the Stern potential. When the adsorption is nearly completed, due to the zero-voltage desorption of the electrode, the overall electric field of the MCDI CDI is weak at this time (120.0 s). The potential distribution falls within the range of 0~0.14 V. At the end of the desorption stage (240.0 s), the positive electrode basically reaches the potential balance and the potential is zero.

5. INFLUENCE OF PARAMETERS ON DESALINATION PERFORMANCE

To evaluate the effects of cell voltage, inlet velocity, channel spacing, thickness of ion exchange membrane and electrode thickness on the desalination performance of MCDI, 3~4 equal differences of each parameter are selected in the appropriate range and the ion adsorption/desorption rates are applied as the evaluation indices of MCDI performance. According to Table 1, the numerical simulation is carried out according to the control variable method under the same conditions of other parameters. The MCDI performance evaluation indices are based on the effluent salt concentration and inlet salt concentration. Among them, the adsorption rate η_1 of the adsorption stage is defined as the difference between the effluent concentration c_{out} and the influent concentration c_{in} divided by the influent concentration c_{in} . Similarly, the desorption rate η_2 of the desorption stage is also defined as previously mentioned.

5.1. Applied voltage influence

To investigate the effect of cell voltage, four voltages are selected as 0.6 V, 0.8 V, 1.0 V and 1.2 V. The end of adsorption is set to 120 s. Figure 6 shows the ion adsorption/desorption rate curves of MCDI units at different voltages.

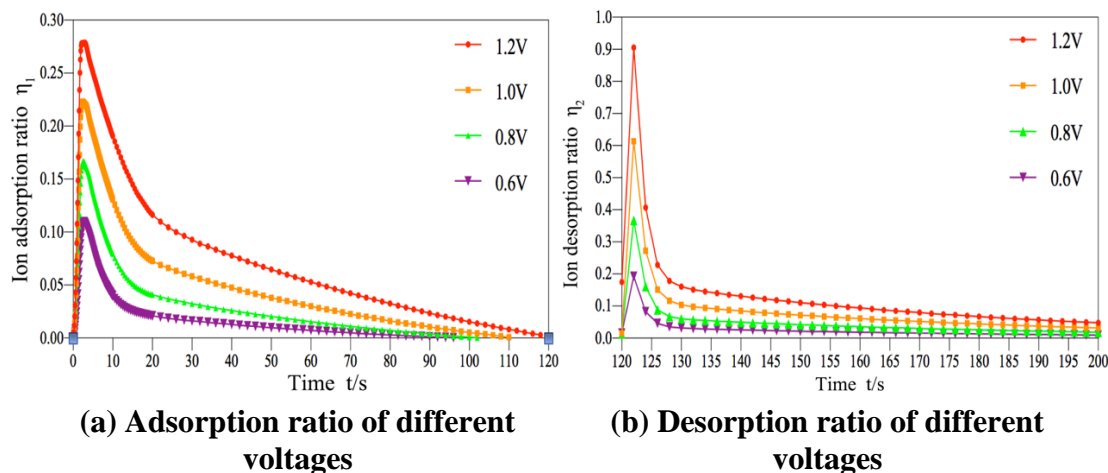


Figure 6. Curves of (a) ion adsorption rate and (b) ion desorption rate at different voltages

Figure 6 shows that as the voltage increases in the voltage variation range of 0.6 to 1.2 V, the electric field between the electrode plates increases, the ion adsorption rate increases, and the adsorption amount of the electrode gradually increases. Moreover, the ion adsorption/desorption rate also stably and uniformly increases at a voltage increase interval of 0.2 V. Since the adsorption principle of the electrode conforms to the GCS-CS electric double layer theory, the larger the cell voltage is, the larger the ion storage of the electric double layer formed on the electrode surface. As the adsorption continues, the ion storage of the electric double layer inside the porous electrode and on the surface of becomes saturated, and the adsorption rate drops to zero. Figure 6 shows that the adsorption voltage of 1.2 V has a maximum adsorption rate of 0.28. In the desorption stage, the variation in the desorption ratio with the cell voltage is consistent with that in the adsorption process. The higher the cell voltage is, the greater the desorption rate and the longer the time needed to complete the desorption process and same conclusions summed in [42].

5.2. Inlet velocity influence

To investigate the effect of inlet velocity, four flow velocities are selected as 0.05 m/s, 0.10 m/s, 0.15 m/s and 0.20 m/s.

The end of adsorption is set to 120 s. Figure 7 shows the ion adsorption rate curve of the absorption stage and the ion desorption rate curve of the desorption stage of the MCDI unit at different flow velocities.

Figure 7 shows that, as the flow velocity decreases from 0.20 m/s to 0.05 m/s, the maximum ion adsorption rate (salt removal rate) increases from approximately 0.15 to more than 0.55. The adsorption amount of the electrode gradually increases. Similarly, the ion desorption rate is also improved to the same extent. In the range of 0.05~0.10 m/s, the range of change is large, while in the range of 0.10~0.20 m/s, the range of change is small and similar results present in [42]. In practical applications, the long retention time caused by the excessively low flow velocity will greatly reduce the amount of purified water per unit time, which will reduce the economics of MCDI. High flow velocity causes a decrease in

the electrode ion adsorption amount and ion absorption and desorption rates. This problem can be solved by increasing the number of MCDI units connected in series, that is, increasing ion migration and mass transfer time to improve purification at high flow rates.

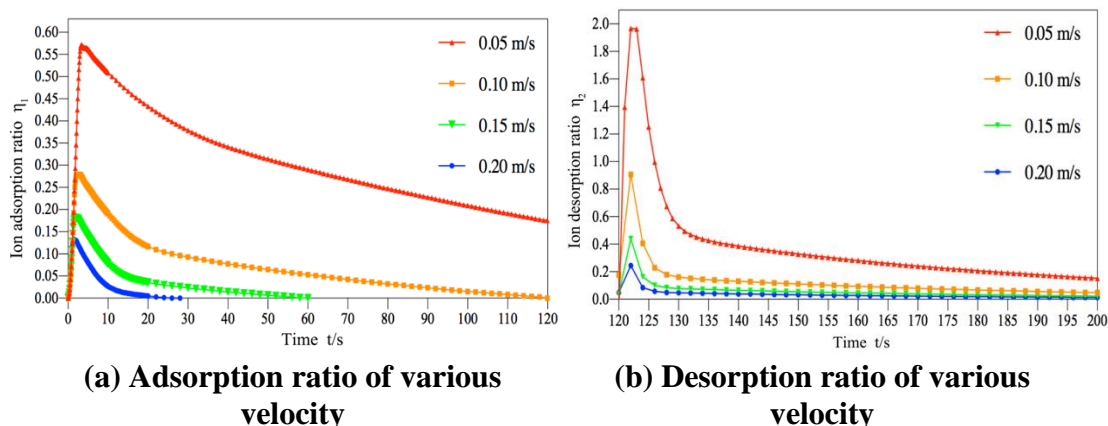


Figure 7. Curves of the (a) ion adsorption rate and (b) ion desorption rate at different current velocities

5.3. Spacer channel size influence

To investigate the effect of spacer size, three spacer sizes are selected as 0.4 mm, 0.8 mm and 1.2 mm. The end of adsorption is set to 120 s. Figure 8 shows the ion adsorption/desorption rate curves of the MCDI unit for different spacer channels.

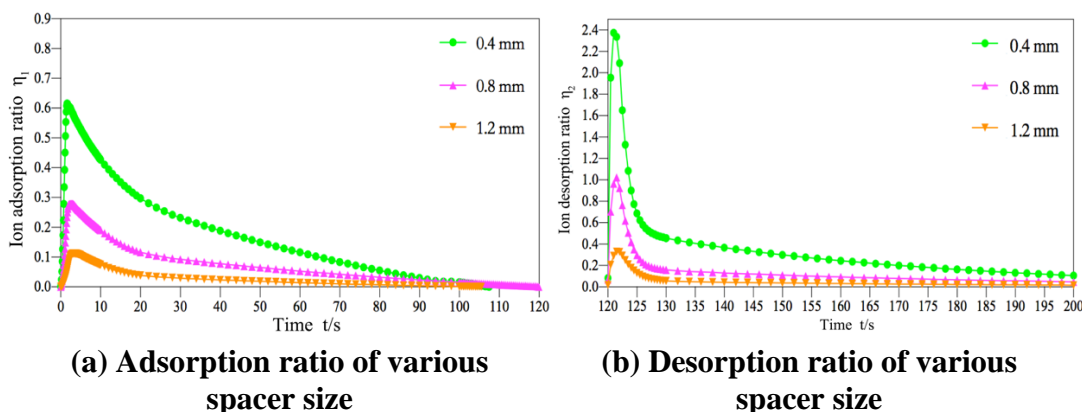


Figure 8. Curves of (a) ion adsorption rate and (b) ion desorption rate for different sizes of spacer channels

Figure 8 shows that the smaller the spacer channel is, the larger the adsorption/ desorption rate is. The variation range is larger in the range of 0.4 to 0.8 mm and the variation range is smaller in the range of 0.8 to 1.2 mm. When the space is 0.4 mm, the maximum adsorption rate can be 0.6. The smaller the spacer channel is, the smaller the distance and resistance that ions in the flow channel need to migrate to the surface of the plate, so the higher the adsorption efficiency. The smaller the spacer channel is, the

greater the electrostatic force in the unit after the cell potential is applied. The ion adsorption capacity of the electric double layer becomes stronger, which enhances the desalination capacity of the electrode. Conversely, as the spacer channel increases, the flow path volume and the diffusion distance of the ions perpendicular to the flow direction increase, and the salt removal rate is greatly reduced.

As analyzed above, to accelerate the removal of salt ions inside the MCDI, the spacer channel should be reduced as much as possible. For example, a flow-through electrode (FTE) structured MCDI unit [43] can be employed, in which the solution no longer flows through the center of the electrode pair but penetrates the pores of the porous electrode by applying pressure. The intermediate channel is no longer the main channel in the FTE-type MCDI unit, so the intermediate channel thickness can be minimized (provided that the electronic isolation is still sufficient), thereby increasing the desalination rate and making the unit structure more compact.

5.4. Ion exchange membrane thickness influence

To investigate the effect of the thickness of the ion exchange membrane, three ion exchange membranes are selected as 0.01 mm, 0.02 mm and 0.03 mm. The end of adsorption is set to 120 s. Figure 9 shows the ion adsorption rate curve in the adsorption stage and the ion desorption rate in the desorption stage of MCDI for different membrane thicknesses.

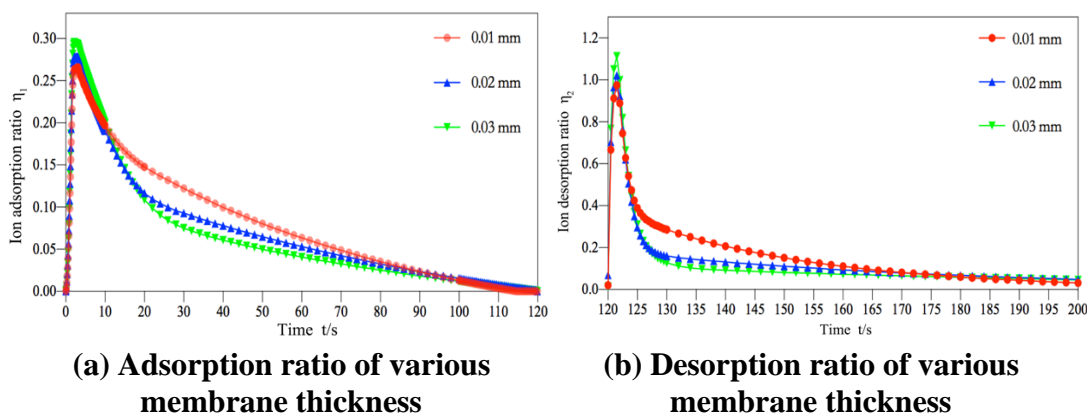


Figure 9. Curve of (a) ion adsorption rate and (b) ion desorption rate at a various membrane thicknesses

Figure 9 shows that in the adsorption stage, the maximum ion adsorption rate increases from 0.26 to 0.29 with an increase in the membrane thickness. However, after 10 s in the adsorption stage, the adsorption rate decreases with an increase in the membrane thickness. In the desorption process, the ion desorption rate of the MCDI unit also increases with the membrane thickness at the beginning of adsorption. However, in the middle stage of desorption, the ion desorption rate of the MCDI unit decreases with an increase in the membrane thickness. When the membrane thickness is large, the Coulomb force driving ion migration will gradually become gentler with an increase in the film thickness. When the membrane thickness is moderate, the Coulomb force driving ion migration will be enhanced

with an increase in the membrane thickness. When the film thickness is small, the Coulomb force that drives ion migration decreases as the membrane thickness increases [31]. The three membrane thicknesses selected in this paper fall within the moderate thickness range, and a higher ion adsorption rate is obtained when a thickness of 0.03 mm is selected. Therefore, selecting a larger thickness of ion exchange membrane within a suitable range of thickness is advantageous for the improvement of the desalination performance of the MCDI.

5.5. Influence of the porous carbon electrode thickness

To investigate the effect of the thickness of the porous carbon electrode, three ion exchange membranes are selected 0.1 mm, 0.2 mm, and 0.3 mm. The end of adsorption is set to 120 s. Figure 10 shows the curves of the ion adsorption rate and ion desorption rate of the MCDI for different electrode thicknesses.

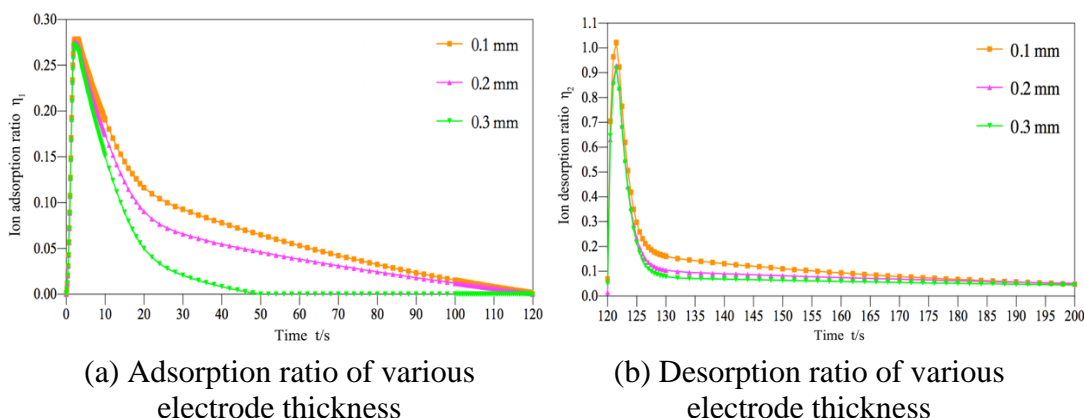


Figure 10. Curves of the (a) ion adsorption rate and (b) ion desorption rate for various electrode thicknesses

Figure 10 shows that in the adsorption stage, the peak value of the ion adsorption rate does not change significantly with an increase in the electrode thickness. The peak value is approximately 0.27 for different thicknesses. However, when adsorption tends to be saturated, the adsorption rate of 0.1 mm electrode thickness is significantly better than that of the 0.3 mm electrode thickness. The adsorption rate decreases as the electrode thickness increases. In the desorption process, the desorption rate of the 0.1 mm electrode thickness is also significantly better than that of the other two thicknesses. When the thickness of the porous carbon electrode is increased, not only do the migration distance and migration resistance of ions diffused inside the electrode increase but also, the resistance of the electrode itself increases [44]. Therefore, a porous electrode should have a smaller thickness in the appropriate range of electrode thicknesses (for example, a thickness of 0.1 mm is selected in this paper). The diffusion rate that is conducive to the stable migration of ions is not too small, and the internal adsorption capacity exerts a large effect, thereby enhancing the adsorption effect.

6. CONCLUSION

In this paper, the prediction of the internal dynamical behavior of MCDI is demonstrated to be inaccurate with the classical GCS model of EDL theory, thus the CS state equation accounting for the finite ion size effect is employed to modify the GCS model, and applied to the multifield coupling numerical simulation. The result shows that the modified model works better than the classical model in terms of both predictability and predictive accuracy. Since the overestimation of the amount of removed ions by the classical model is corrected, the minimum value of the effluent concentration curve of the modified model increases by approximately 20mol/m^3 , and the rate of rise is gradually reduced when the ion concentration tends to achieve balance at the end of adsorption. The modified model also corrects the concentration curve of desorption. The modified GCS model is further adopted to investigate the desalination performance of MCDI. It is demonstrated that the performance is better when the voltage reaches 1.2 V (avoiding the Faraday reaction on the electrode surface), with the ion adsorption ratio reaching the highest, value of 0.28. However, the flow velocity can affect the overall performance of desalination. When the flow velocity increases, it causes a decline in the adsorption ratio, so 0.05~0.10 m/s is a suitable flow velocity range. The wider spacer channel increases the resistance to ion diffusion and migration, but a narrower channel (with a size of 0.4 mm) can increase the ion adsorption ratio to the highest, value of approximately 0.60. In addition, the ion exchange membrane has a minimal effect on the desalination performance due to its small adjustable thickness range. However, if selected moderately (within 0.01~0.03 mm), the Coulomb force driving ion migration increases with an increase in its thickness, which is beneficial to the improvement of the ion adsorption ratio. The change in the thickness of the porous carbon electrode plate mainly affects the adsorption rate in the stage of adsorption tending to saturation. The increase in thickness will increase the diffusion distance and migration resistance of ions in the electrode, and the resistance of the electrode itself, resulting in a decline in adsorption ratio. However, the peak adsorption ratio did not change significantly, and the numerical simulation showed that it remained at approximately 0.27.

ACKNOWLEDGEMENTS

This research was funded by National Natural Science Foundation of China, grant number 51906091, and by Natural Science Research of Jiangsu Higher Education Institutions of China, grant number 19KJB470019 and 20KJD470001.

References

1. Y. Tong, S. Zhou, J. Zhou, G. Zhang, X. Li, C. Zhao and P. Liu, *Water Reuse*, 11 (2021) 189.
2. B. Spa, C. Rza, C. Avdw, E. Vpd and C. Pmba, *Prog. Mater. Sci.*, 58 (2013) 1388.
3. M. Suss, S. Porada, X. Sun, M. Biesheuvel and V. Presser, *Energy Environ. Sci.*, 8 (2015) 2296.
4. E. Avraham, M. Noked, Y. Bouhadana, A. Soffer and D. Aurbach, *J. Electrochem. Soc.*, 156 (2009) 95.
5. T. Ci, J. E. Dykstra and S. Porada, *J. Colloid Interface Sci.*, 446 (2015) 317.
6. H. Li, G. Yang, L. Pan, Y. Zhang, Y. Chen and S. Zhuo, *Water Res.*, 42 (2008) 4923.
7. J. B. Lee, K. K. Park, H. M. Eum and W. C, *Desalin.*, 196 (2006) 125.
8. P. M. Biesheuvel and A. Wal, *J. Membr. Sci.*, 346 (2010) 256.

9. A. Omosebi, X. Gao, J. Landon and K. Liu, *ACS Appl. Mater. Interfaces*, 6 (2014) 12640.
10. P. A. Fritz, F. K. Zisopoulos, S. Verheggen, K. Schro N and R. M. Boom, *Desalin.* 444 (2018) 162.
11. P. M. Biesheuvel, R. Zhao, S. Porada and A. V. D. Wal, *J. Colloid Interface Sci.*, 360 (2011) 239.
12. P. Decalogue, B. Anet, S. J. Metz, K. Nijmeijer and M. Wessling, *J. Membr. Sci.*, 346 (2010) 163.
13. Y. J. Ci and J. H. Choi, *Sep. Purif. Technol.*, 71 (2010) 70.
14. J. H. Lee and J. H. Choi, *J. Membr. Sci.*, 409 (2012) 251.
15. W. Tang, D. He, C. Zhang, P. Kovalsky and T. D. Waite, *Water Res.*, 120 (2017) 229.
16. A. Hassanvand, G. Q. Chen, P. A. Webley and S. Kentish, *Water Res.*, 131 (2018) 100.
17. Y. Jande and W. S. Kim, *Sep. Purif. Technol.*, 115 (2013) 224.
18. J. Y. Lee, S. J. Seo, S. H. Yun and S. H. Moon, *Water Res.*, 45 (2011) 5375.
19. Y. J. Ci, J. H. Kim and J. H. Choi, *J. Membr. Sci.*, 429 (2013) 52.
20. N. S. Kwak, S. K. Jin, T. S. Hwang and E. M. Choi, *Desalin.*, 285 (2012) 138.
21. Y. Li, Y. Liu, J. Shen, J. Qi, J. Li, X. Sun, J. Shen, W. Han and L. Wang, *Desalin.*, 430 (2018) 45.
22. A. Hassanvand, G. Q. Chen, P. A. Webley and S. E., *Desalin.*, 417 (2017) 36.
23. M. Andelman, *Sep. Purif. Technol.*, 80 (2011) 262.
24. P. M. Biesheuvel, H. Hamelers and M. E. Suss, *Colloids Interface Sci. Commun.*, 9 (2015) 1.
25. M. W. Salem and W. S. Kim, *Desalin.*, 437 (2018) 133.
26. S. G. Yao and J. W. Wu, *Desalin. Water Treat.*, 144 (2019) 1.
27. R. Burt, G. Birkett and X. S. Zhao, *Chem. Phys.*, 16 (2014) 6519.
28. S. Vasani, C. D. Bain, R. W. Field and Z. Cui, *Desalin.*, 200 (2006) 175.
29. H. Helmholtz, *Ann. Phys.*, 165 (1853) 353.
30. Y. Song, E. A. Mason and R. M. Stratton, *J. Phys. Chem.*, 93 (1989) 6916.
31. J. J. López-García, J. Horno and C. Grosse, *J. Colloid Interface Sci.*, 428 (2014) 308.
32. Carnahan and F. Norman, *J. Chem. Phys.*, 51 (2003) 635.
33. H. K. Mutha, H. J. Cho, M. Hashempour, B. L. Wardle, C. V. Thompson and E. N. Wang, *Desalin.*, 437 (2018) 154.
34. R. Liu, S. Yao, Y. Li and J. Cheng, *Int. J. Heat Mass Transfer*, 135 (2019) 769.
35. D. Roshanak, M. Ali and B. Mostafa, *Anal. Chim. Acta*, 1158 (2021) 338414.
36. A. Hemmatifar, M. Stadermann and J. G. Santiago, *J. Phys. Chem. C*, 44 (2015) 24681.
37. H. Li, L. Pan, Y. Zhang, L. Zou, C. Sun, Y. Zhan and S. Zhuo, *Chem. Phys. Lett.*, 485 (2010) 161.
38. S. Zhu, J. Yu, T. C. Stewart and H. L. Tang, *AWWA Water Sci.*, 1 (2019) e1166.
39. H. Tun and C. C. Chen, *Adsorption*, 27 (2021) 979.
40. N. Kim, E. A. Lee, X. Su and C. Kim, *Desalin.*, 503 (2021) 114950.
41. P. Soo-Kyung and C. Jae-Hwan, *Sep. Purif. Technol.*, 209 (2019) 152.
42. W. Xiaobing, L. Jinqiu, L. Yang, L. Sen, L. Dong, M. Tingting, J. An, H. Yanshe and G. Fengwei, *Water Air Soil Pollut.*, 232 (2021) 1.
43. E. N. Guyes, A. N. Shocron, A. Simanovski and P. M. Biesheuvel, *Desalin.*, 415 (2017) 8.
44. S. Porada, M. Bryjak, A. Van Der Wal and P. Biesheuvel, *Electrochim. Acta*, 75 (2012) 148.